Sedimentation of a suspension of paramagnetic particles in an external magnetic field

Jérémy Vessaire, Nicolas Plihon, Romain Volk, and Mickaël Bourgoin
Univ Lyon, ENS de Lyon, Univ Claude Bernard Lyon 1, CNRS, Laboratoire de Physique, F-69342 Lyon, France

(Received 10 May 2019; accepted 3 July 2020; published 3 August 2020)

We investigate the sedimentation of initially packed paramagnetic particles in the presence of a homogeneous external magnetic field, in a Hele-Shaw cell filled with water. Although the magnetic susceptibility of the particles is small and the particle-particle-induced magnetic interactions are significantly smaller compared to the gravitational acceleration, we do observe a measurable reduction of the decompaction rate as the amplitude of the applied magnetic field is increased. While induced magnetic dipole-dipole interactions between particles can be either attractive or repulsive depending on the particles relative alignment, our observations reveal an effective overall enhancement of the cohesion of the initial pack of particles due to the induced interactions, very likely promoting internal chain forces in the initial pack of particles. The influence of the magnetic field on the particles once they disperse after being decompacted is, however, found to remain marginal.

DOI: 10.1103/PhysRevE.102.023101

I. INTRODUCTION

The present study is motivated by the general topic of transport of particles in flows, which is of broad interest for fundamental scientific issues, industrial applications, and natural systems. In nature, the formation of rain droplets in clouds, pyroclastic flows, dispersion of pollutants in the atmosphere, or planet formation in accretion disks are just a few examples. In industrial applications, one can mention spray combustion in diesel engines, fluidized beds, pneumatic transport of granular media, or mixing processes. Most of these situations are quite complex due to the turbulent nature of the carrier flow, or to the fact that they are densely seeded, which makes the coupling between the particle dynamics and the flow random and multiscale.

When it comes to the modeling of such particle laden flows, several situations must be distinguished depending on (i) the nature of the particles, and (ii) their local concentration. In a very dilute situation, with sufficiently small particles, a point-wise approximation is relevant so that the dynamics of the particles is well captured by the celebrated Maxey-Riley-Gatignol equation [1]. In the recent years, experimental and direct numerical simulations studies of turbulent transport proved this approach to be valid, providing that the particle size is of the order of the smallest length-scale in the flow [2–6]. When the particle mass fraction is no longer negligible as compared to the one of the fluid, both the fluid and particles are fully coupled so that one has to resolve the flow around moving objects from first principles [7,8], or to model the mixture as a continuous medium [9–11]. This situation corresponds for instance to dense suspensions which exhibit non trivial behaviors even in very simple configurations such as sedimentation [12,13] or gravity currents [14]. Indeed, the rheology of such complex systems is strongly influenced by interparticle interactions, which can lead to strong fluctuations even at moderate Reynolds number [15].

In this broad context of inertial particle laden flows, the present work is a preliminary study in a long-term perspective aiming at addressing more particularly the role played by particle-particle interactions on the dynamics of particulate systems at high volume fraction. Such interactions are common in fluidized beds, or natural systems such as clouds, where water droplets tend to be charged.

To improve our understanding of the role played by the many possibly coupled phenomena above mentioned, it is wise to go step by step and consider first simpler situations to disentangle possible individual contributions of the different effects, before considering the fully coupled situation. In the present article, we therefore focus on some basic aspects of the role played by particle-particle interactions, considering the simplified situation where the flow is initially at rest and the particles are initially packed and also at rest. More precisely, we investigate in a Hele-Shaw cell the sedimentation of paramagnetic particles subjected to gravity and to a tunable external homogeneous magnetic field perpendicular to gravity. The interest of using paramagnetic particles relies on the fact that the—dipole-dipole—interactions between particles can be directly tuned by adjusting the amplitude of the applied magnetic field. The chosen configuration for this preliminary study, with initially packed particles in a fluid at rest aims at considering first the most favorable situation regarding the possible impact of magnetic forces. The choice of such a configuration somehow moves the original motivation in the context of particle-laden flows, to the field of granular physics, where we investigate the decompaction of a granular system of sub-millimetric particles with tunable interactions. Interestingly, beyond our longterm goal in the context of particle laden flows, this opens new perspectives for future dedicated studies with the same experimental setup to address interesting questions in the field of granular and deformable porous media.

Figure 1 represents a time series of the investigated decompaction and sedimentation process. The situation is relatively canonical in the context of granular media research. Over the last decades, numerous studies have indeed investigated the sedimentation of such a granular pack in newtonian fluids

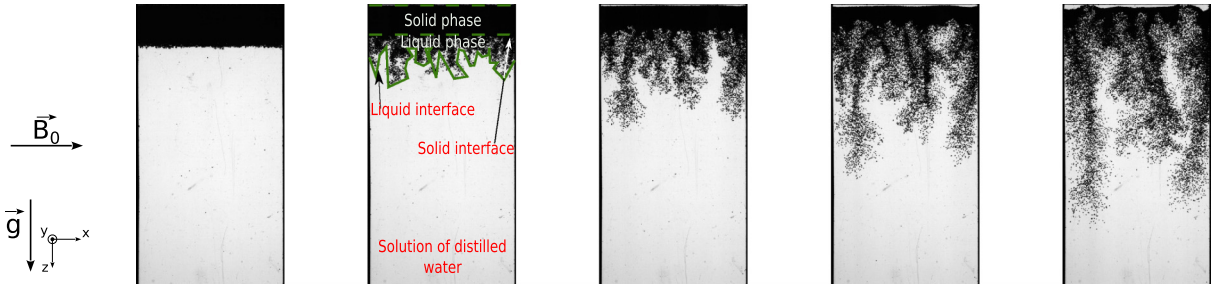

(a) t = 0s (b) t = 1s (c) t = 2s (d) t = 3s (e) t = 4s

FIG. 1. Temporal series of images showing sedimentation subjected to gravity and a horizontal magnetic field in a steady flow with 250 μm diameter paramagnetic particles in a closed Hele-Shaw cell. The cell is 200 mm high, 50 mm wide, and 1 mm depth. The cell is illuminated with a backlight, such that particles appear as dark spots on the original images.

[16–21]. The question of the nature and the dynamics of interface instabilities in the early stage of the decompaction has received particular interest. Notably, the emergence of a fingering instability has been demonstrated, recalling the well-known Rayleigh-Taylor instability which classically develops at a horizontal interface between two fluids with different densities (the denser being on top) [22,23]. Several authors have investigated theoretically and experimentally the fingering instability of the particle pack and fluid interface in a Hele-Shaw cell [19–21], proposing fluid interpretation a la Rayleigh-Taylor.

The present study does not address the fingering instability but focuses on characterizing the decompaction and fluidization rate of the particles pack when magnetic interactions are present. These interactions are driven here by the induced magnetization of the particles by the external field and are of the type *induced dipole-induced dipole*. As such, depending on the relative position and alignment of the particles, the interactions can be either attractive or repulsive. It is therefore unclear, *a priori*, whether they will contribute to an increased cohesion of the pack of particles or on the contrary they will accelerate its decompaction. Besides, considering the small value of the magnetic susceptibility of the paramagnetic particles considered, it is also *a priori* unclear whether a measurable influence of the additional particle-particle magnetic interactions could be detected.

The article is organized as follows: in Sec. II we present the overall process of sedimentation of paramagnetic particles and the possible relevant dimensionless parameters of the problem; in Sec. III we describe the experimental setup; Sec. IV presents the main results, showing the impact of particle-particle interactions on the decompaction rate. The article ends with a brief discussion of the observed trends and possible perspectives of this work both in the context of particle laden flows and granular media.

II. SEDIMENTATION OF PARAMAGNETIC PARTICLES WITH AN APPLIED EXTERNAL MAGNETIC FIELD

We briefly describe here the investigated decompaction and sedimentation process of dense particles in water as illustrated in Fig. 1 for one single typical realization. Particles are small (250 μm in diameter) monodisperse spherical beads with density $\rho_p = 1.2$ g/cm^3. After the particle pack is prepared to get a horizontal interface by vibrating the cell with particles initially placed at its bottom (see Sec. III for further details on the preparation step), the Hele-Shaw cell is quickly rotated around the horizontal axis to bring the pack upwards. The time origin ($t = 0$ s) is defined when the cell reaches the vertical position with the particle pack on top. On the first frame [Fig. 1(a)], we see the initial pack of particles, standing above water (note that the particles are fully permeated with water). The shape of the "particle-bed and water" interface is nearly flat and horizontal. On the next three frames [Figs. 1(b)–1(d)], showing the subsequent decompaction and sedimentation of the particles, two main regions can be defined for the particle suspension: (i) in the upper part, particles remain packed and form a homogeneous and compact pack at rest, (ii) below, the interface is disturbed giving rise to fingers of dispersed sedimenting particles. Following classical granular *terminology* [13], we shall call *solid* phase the upper compact region of particles and *liquid* phase the lower sedimenting region. We therefore distinguish two interfaces: (i) the first between the *solid* and *liquid* phases of particles, (ii) the second between the *liquid* phase of particles and water. As the sedimentation process goes on, the volume of the *solid* phase reduces (we shall refer to this as the *decompaction* or the *liquefaction* of the solid phase) and at the same time the area of the *liquid* interface increases (the solid-liquid interface slowly moves up while the liquid-water interface develops larger fingers). Note that, as the total number of particles in the system is conserved, and since particles initially in the compact *solid* phase liquefy into the less compact *liquid* phase, the total area occupied by the particles grows in time during the *decompaction* process. In the last frame [Fig. 1(e)], the solid phase has totally *melted* and disappeared. As the *liquid* fingers of particles develop further, the dynamics of the suspension becomes strongly influenced by the induced re-circulation flow of water in the cell and by lateral confinement effects due to the finite size of the cell.

In the present work we focus on the dynamics of the initial decompaction process ($t \lesssim 3$ s) and do not address specific long-term effects which are strongly affected by the finite size of the cell [24]. We investigate the liquefaction rate of the *solid* phase as well as the growth rate of the *liquid*phase, with the goal to highlight the impact of particle-particle interactions on the global sedimentation behavior, when imposing a tunable homogeneous horizontal magnetic field $\vec{B}_0 = B_0\vec{x}$, with $\vec{x}$ the

horizontal direction along the width of the Hele-Shaw cell and $\vec{z}$ the vertical direction such that gravity acceleration is $\vec{g} = g\vec{z}$.

In the absence of any external magnetic field ($B_0 = 0$ G), particles are only subjected to gravity $\vec{g}$ (and eventually hydrodynamic interactions).

In the presence of a homogeneous magnetic field ($B_0 \neq 0$ G), all particles acquire an identical induced magnetic moment $\vec{M}$ given by

$$\vec{M} = \frac{4}{3}\pi r^3 \frac{\chi_m}{\mu_0}\vec{B}_0, \tag{1}$$

where r is the radius of the particles, μ_0 the vacuum permittivity, and χ_m the magnetic susceptibility of the particles. In addition to gravity, each particle is then subjected to the magnetic force exerted by the magnetization of the other particles. The magnetic force $\vec{f}_m^i$ acting on particle i can then be written as

$$\vec{f}_m^i = (\vec{M}_i \cdot \vec{\nabla})\vec{B}_i, \tag{2}$$

where $\vec{M}_i$ is the induced magnetization of particle i and $\vec{B}_i = \vec{B}_0 + \sum_{k\neq i}^{N_p} \vec{b}_{ki}$ the total magnetic field at the position of particle i, including both the applied field $\vec{B}_0$ and the total induced magnetic field $\vec{b}_i = \sum_{k\neq i}^{N_p} \vec{b}_{ki}$ from all other particles than i. Note that as we consider here the case of a homogeneous applied magnetic field $\vec{B}_0$, there is no net force exerted by $\vec{B}_0$ on the magnetized particles and f_m^i is simply given by

$$\vec{f}_m^i = (\vec{M}_i \cdot \vec{\nabla})\vec{b}_i. \tag{3}$$

We recall that the dipolar magnetic field $\vec{b}_{ki}$ generated by a particle k with magnetization $\vec{M}_k$ at the position of particle i is given by

$$\vec{b}_{ki} = \frac{\mu_0}{4\pi}\left(\frac{3\vec{r}_{ki}(\vec{M}_k \cdot \vec{r}_{ki})}{|\vec{r}_{ki}|^5} - \frac{\vec{M}_k}{|\vec{r}_{ki}|^3}\right), \tag{4}$$

where $\vec{r}_{ki}$ is the separation vector between particle k and particle i. Considering the rapid decay of $\vec{b}_{ki}$ with $|\vec{r}_{ki}|$, contributions to $\vec{b}_i$ mostly come from the nearest neighbors, which in the initially compact pack are at a distance $\vec{r}_{ki}$ commensurate with the particle diameter $d = 2r$ (although the orientation—repulsive or attractive—of the force changes depending on the position of the considered neighbors around particle i). As a consequence, the typical expected order of magnitude for $|\vec{b}_i|$ is given by $\mu_0 M/4\pi r^3$, and considering Eqs. (1) and (3), the typical order of magnitude of the magnetic force is

$$\mathcal{O}\left(|\vec{f}_m^i|\right) \propto \frac{r^2\chi_m^2 B_0^2}{\mu_0}. \tag{5}$$

Based on these estimates, we can then define a dimensionless number Ψ comparing the amplitude of particle-particle magnetic force and gravity (including effect of buoyancy) acting on each particle:

$$\Psi = \frac{\chi_m^2 B_0^2}{\mu_0 r|\rho_p - \rho_w|g}, \tag{6}$$

with ρ_p and ρ_w the density of the particles and of water, respectively. We shall refer to Ψ as the *magneto-gravitational* number.

III. EXPERIMENTAL SETUP

Experiments were performed in a sealed Hele-Shaw cell (200 mm in height, 50 mm in width, with a gap of 1 mm), filled with distilled water and paramagnetic particles. A small amount of surfactant (Sodium dodecyl sulfate) is also added to stabilize the solution and to prevent aggregation of the particles. Figures 2(a) and 2(b) show a schematic of the cell and a typical recorded image of settling particles. The gap of the Hele-Shaw cell is fixed by a thin (1 mm in thickness) internal plastic frame clamped between two plexiglass plates. Two pivots screwed on the sides of the cell at mid-height allow to rotate the cell around the horizontal axis $\vec{x}$.

As particles, we used 250 μm (in diameter) polythene (PE) microspheres, with density $\rho_p = 1.2$ g. cm^{-3} doped with iron oxyde (FeO) to be paramagnetic (BKPMS particles from Cospheric LLC, Santa Barbara, CA). We have determined their magnetic susceptibility χ_m from a SQUID magnetometer measurement on individual particles, carried at the CML (Center of Magnetometry of Lyon), leading to a value $\chi_m \simeq 4.2 \times 10^{-3}$.

Two coils in Helmholtz configuration surround the cell to apply a homogeneous horizontal magnetic field $\vec{B}_0$, parallel to the x axis, aligned with the width of the cell (Fig. 2). The water-cooled coils are driven with a 10 kW power supply (Danfysik System 9100). The maximum amplitude of the applied magnetic field is $B_0^{\max} \approx 0.12$ T. It is turned on during all runs and is therefore applied during the iniatilization protocol of the particle pack described in next paragraph.

To carry out a systematic investigation with good statistical convergence, for a given value of the applied magnetic field, of the order of 50 sedimentation experiments are repeated with the same initialization protocol. For a good reproducibility of experimental conditions, the setup is fully automatized, the rotation been ensured by a stepper motor controlled from a Raspberry Pi nanocomputer with a preprogrammed cycle. Special care has been taken to properly condition the initial pack of particles in between rotations to have a particle-bed and water interface as flat and horizontal as possible before each rotation. This is achieved by applying to the cell several rapid oscillations and simultaneously vibrating the cell with an electrodynamic shaker. This optimal pack conditioning protocol is also automatized (and is part of the global rotation cycle controlled by the nanocomputer) and warrants that the exact same protocol is applied for every experiment. Note that in spite of this care, the initial compaction of the particle bed may still present some variations from one realization to another. To limit any bias due to such variations of initial conditions, we remove from the ensemble of realizations those for which the initial height of the particle bed deviates from the average height by more than 10%. This ensures considering realizations with almost identical initial compaction. As a consequence of this selection, of the order of 15% of the realizations are dropped.

Measurements are based on high-speed backlight imaging of the cell, which is illuminated from behind by a LED panel. Recordings are performed using a high-speed camera (Flare 2M360-CL from IO Industries) operated with a resolution of 2048×1088 pixels at a frame rate of 300 fps. The starting of the recordings is triggered by the controller nanocomputer and is synchronized with the rotation cycle.

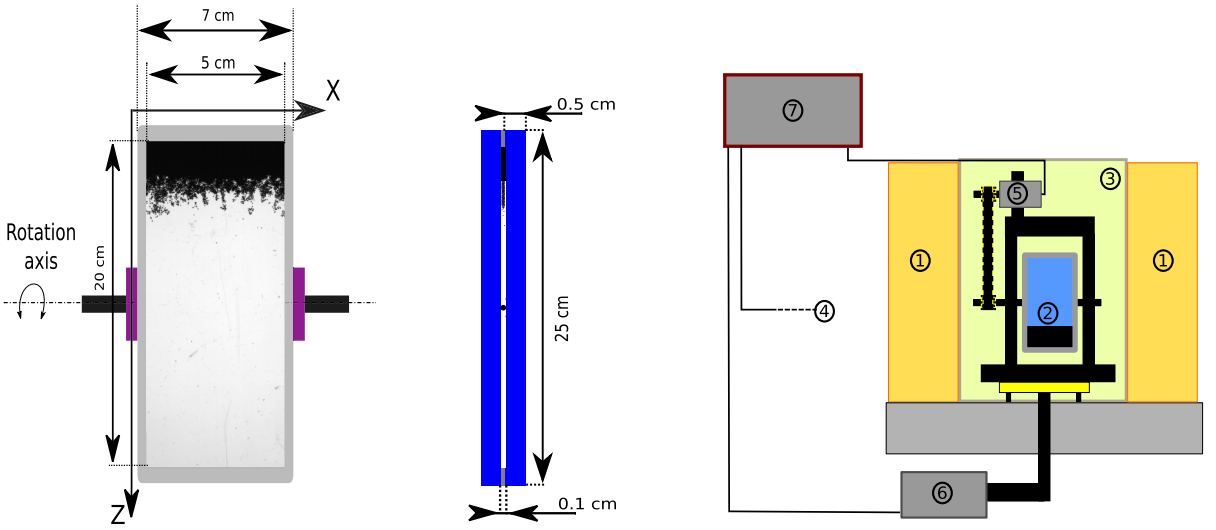

(a) Hele-Shaw cell, front view (b) Hele-Shaw cell, side view (c) Global experimental setup

FIG. 2. (a) Front and (b) side views of the Hele-Shaw cell and (c) automated experimental setup with magnetic coils (1), Hele-Shaw cell (2), backlight LED panel (3), high-speed camera (4), stepper motor (5), shaker (6), and Raspberry-Pi controller (7).

IV. EXPERIMENTAL RESULTS

We present in this section results on the *liquefaction* rate of the *solid* phase and the simultaneous growth of the *liquid* phase of the suspension in the early stage of the sedimentation, right after the cell reaches its vertical position.

We recall here the phenomenology introduced in Sec. II: the particles, initially packed and forming a compact *solid* phase, gradually feed a lower, dilute, *liquid* phase. It is important to note here that the phase classification follows the granular *terminology* [13] and that the *liquid* phase may indeed be compressible. The goal of the present study is to address the dynamics of the granular phases and, in particular, the influence of the magnetogravitational number Ψ on the time evolution of the areas of the *liquid* phase A_l and of the *solid* phase A_s as the decompaction process goes on. The most important results being that (i) interparticle interactions foster the liquefaction rate during the initial phase, while (ii) they mitigate the terminal liquefaction rate, and iii) after a initial strongly compressible transient of the *liquid* phase, the *liquid* phase is about four times more dilute than the *solid* phase, regardless of the intensity of the interparticles interactions. These experimental results, reported in the remaining of this section, have been obtained following a careful and systematic image processing to detect the solid and liquid phases, detailed in next subsection.

A. Edge detection and area calculation

The successive image processing steps are illustrated in Fig. 3 for one specific frame of one realization, at time $t \sim 1$ s (note that, compared to previous figures, negative images are shown, particles appear now as bright). Figure 3(a) shows a raw image, where the *solid* phase appears as a continuous bright region on the top whereas the *liquid* phase is characterized by some fragmentation of the intensity pattern below. Our simple image processing algorithm aims at providing a robust segmentation algorithm to detect three fully connected regions: the (granular) *solid* phase, the (granular) *liquid* phase and the clear water. We first apply a Gaussian low-pass filter to blur the image in the liquid phase: as a result (i) nearby particles in the fragmented region become connected and (ii) the locally smoothed intensity in the *liquid* region decreases as shown in Fig. 3(b). We use a Gaussian convolution kernel with a width of 1.5 particle diameter to reconnect the fragmented areas up to this scale [25]. Few blobs of particles separated by more than 1.5 d can still be present; those will be considered as having already left the *liquid* phase and are excluded from the detection. Note that the Gaussian filtering has no major effect on the *solid* phase region of the image which has constant and homogeneous intensity. Then, two successive thresholdings of the image are operated. The first uses a relatively low threshold chosen to keep all the particles (nondark pixels) in both *solid* and *liquid* phases and segment them from

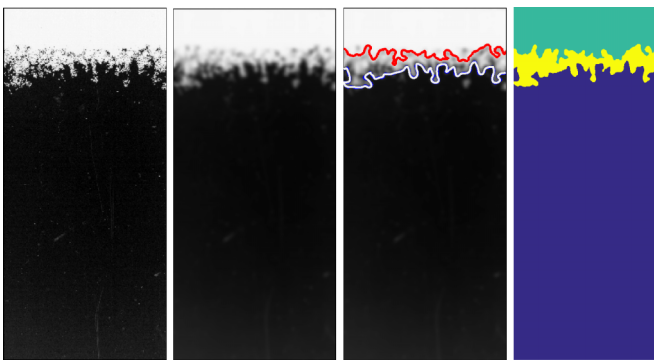

(a) Raw image (b) Low-pass filtered image (c) Egdes detection (d) Ternarized image

FIG. 3. Successive steps of image processing to determine the *solid* phase [upper green area in (d)] and *liquid* phase [middle yellow area in (d)] of particles starting from the raw image (a).

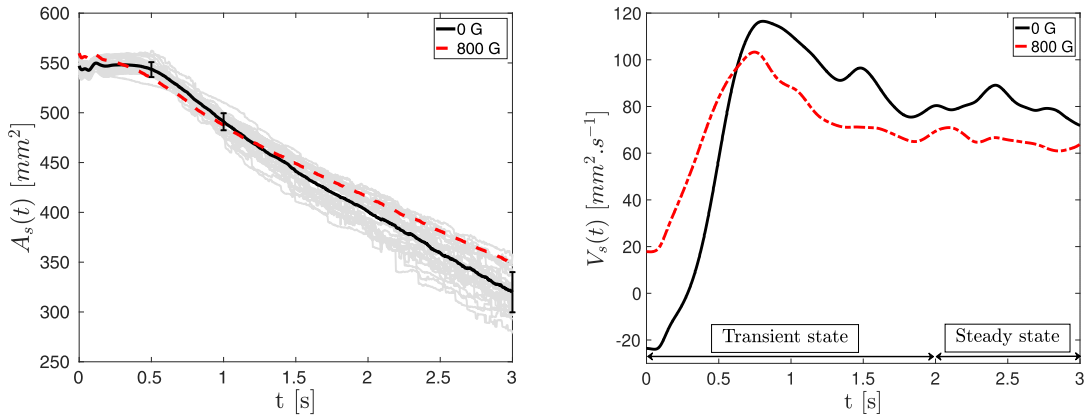

(a) Mean area versus time (b) Mean velocity versus time

FIG. 4. (a) Averaged time evolution of the solid area without any applied magnetic field (solid black line) and with an applied field with amplitude $B_0 = 800$ G (dashed red line, corresponding to a magnetogravitational number $\Psi \simeq 0.26$). To illustrate the averaging procedure, the light gray lines represent the individual time evolution of the solid area for 50 independent realizations for the case without any applied magnetic filed. The solid black line correspond to the average of the light gray lines. The bars at 0.5 s, 1 s, and 3 s indicate the standard deviation among the 50 realizations at each of these instants. (b) Time evolution of the *liquefaction* velocity for $B_0 = 0$ G (solid black line); $B_0 = 800$ G (dashed red line).

the pure water phase. An edge detection algorithm is then run on the binarized image to determine the *liquid*-water interface [blue line in Fig. 3(c)]. The second thresholding uses a higher value of the threshold, chosen to keep only the bright pixels in the continuous region corresponding to the *solid* phase and segment it from the *liquid* phase. Another edge detection then retrieves the *solid-liquid* interface [solid red line in Fig. 3(c)]. The two different binarized images can also be combined to create a ternarized image showing the *solid* phase [upper green region in Fig. 3(d)], the *liquid* phase [middle yellow region in Fig. 3(d)] and water [lower blue region Fig. 3(d)].

This image processing sequence is performed for all frames at time t of each recording during run k, to monitor the time evolution of the areas $A_s^k(t)$ and $A_l^k(t)$ of the *solid* and *liquid* phases, respectively. In the sequel, for a given experiment (i.e., a given value of the applied magnetic field amplitude B_0) we investigate the time evolution of the *solid* and *liquid* phase areas ensemble-averaged over the full set of realizations:

$$\langle A_{s,l}\rangle(t) = \frac{1}{N_{\text{movie}}} \sum_{k=1}^{N_{\text{movie}}} A_{s,l}^k(t - t_{0,k}), \tag{7}$$

with N_{movie} the total number of movies (realizations) recorded for each experiment (N_{movie} being of the order of 50 for each value of applied magnetic field amplitude B_0), and $t_{0,k}$ the instant when the cell reaches its vertical orientation after rotation during run number k. For the sake of clarity, we shall omit from now the average brackets when presenting the results and simply refer to $A_{s,l}(t)$ for the ensemble-averaged areas of the *solid* and *liquid* phases.

B. Liquefaction dynamics and particle concentration

1. Evolution of solid and liquid phases

Figure 4(a) shows the time evolution of the *solid* phase area $A_s(t)$ for the case without any applied magnetic field ($B_0 =$ 0 G) and for the case with $B_0 = 800$ G ($\Psi \simeq 0.26$). A common pattern can be seen, after a short period (of the order of 300 ms) with almost no apparent evolution, where a rapid decrease of $A_s(t)$ occurs followed by a slower linear decrease. A first visible impact of the magnetic field appears in the long term behavior, where we see that the *solid* phase *liquefies* slower in the presence of an applied magnetic field. At $t = 3$ s we observe indeed that the remaining area of *solid* phase is the largest for $B_0 = 800$ G and the smallest when no magnetic field is applied.

To further characterize the influence of the magnetic field on the acceleration/deceleration of *liquefaction* we introduce the *liquefaction rate*:

$$V_s(t) = -\frac{dA_s(t)}{dt}. \tag{8}$$

Note that V_s has units of m^2s^{-1}. Figure 4(b) shows the time evolution of the *liquefaction* rate. Two regimes are clearly visible: after a short transient with a rapid increase of the *liquefaction* rate followed by a local maximum, a constant asymptotic terminal value V_s^∞ is reached. It can be noted that in spite of the large number of recorded movies for each experiment, while the raw curves for $A_s(t)$ appear relatively smooth and well converged, their derivative still exhibit some visible noise. We therefore estimate V_s^∞ by averaging $V_s(t)$ typically on the time interval $t \in [2\text{ s} - 3\text{ s}]$.

During the initial transient of the liquefaction, a systematic trend can be observed where the larger the magnetic field, the larger the *liquefaction* rate. Moreover, we find that the initial liquefaction rate without magnetic field is negative as opposed to the case with an applied magnetic field. This is related to the fact that in absence of magnetic field ($B_0 = 0$ G), magnetic interactions between particles are absent so that the initial pack obtained by vibrating the cell is the most compact, leading to a slightly smaller initial value of A_s. As a consequence, when no magnetic field is applied, the solid phase slightly expands at short time due to small relative motions of the beads. The mild

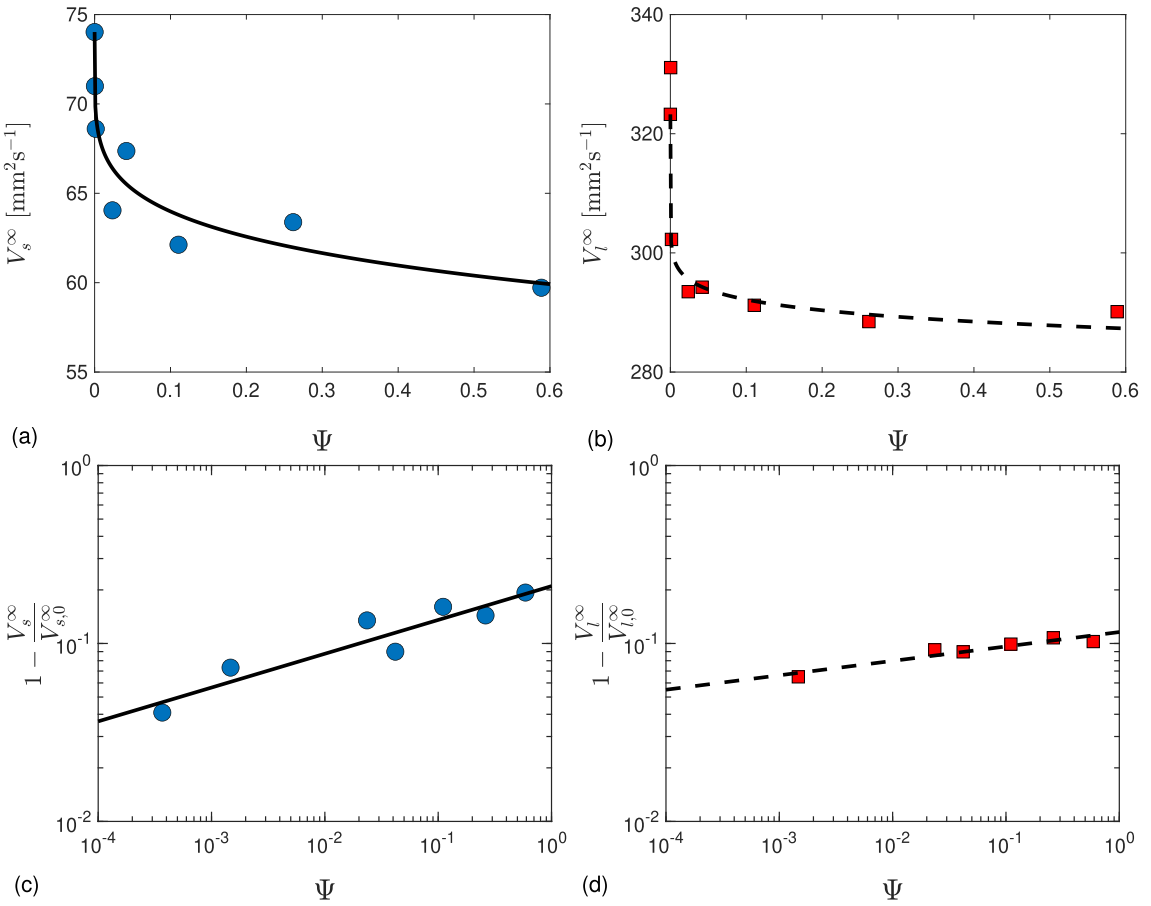

FIG. 5. (a) Terminal *liquefaction* rate of the *solid* phase and (b) terminal growth rate of the *liquid* phase as a function of the magnetogravitational number Ψ. (c) Relative liquefaction for the *solid* phase and (d) growth rate for the *liquid* phase, as a function Ψ. Solid and dashed lines correspond to the power-law fit Eq. (10).

overshoot preceding the terminal regime occurs at a similar time $t \approx 0.7$ s regardless of the amplitude of the magnetic field, although it seems slightly more peaked as the amplitude of the magnetic field increases.

Concerning the terminal *liquefaction* regime, Fig. 5(a) shows the *liquefaction* average terminal rate V_s^∞ as a function of the magnetogravitational number. In agreement with the qualitative observed trend of $A_s(t)$, we see that, in spite of some scatter, the terminal *liquefaction* rate of the *solid* phase globally decreases when the magnetic field increases.

A similar analysis has been performed for the growth of the *liquid* phase, defining the *liquid* growth rate as

$$V_l(t) = \frac{dA_l(t)}{dt}. \tag{9}$$

Figure 5(b) shows the *liquid* average terminal growth rate as a function of the magnetogravitational number. Trends similar to those of the *liquefaction* of the *solid* phase are observed, with a global decrease of the *liquid* growth rate as the magnetic field increases.

The observed trends for the *solid* and the *liquid* phases show consistently that as the magnetic field amplitude increases, the *solid* phase is stabilized (in the sense that it *liquefies* slower) while the *liquid* phase is less supplied with particles and hence it also grows slower. To further characterize the trends of the terminal liquefaction rate of the *solid* phase and the terminal growth rate of the *liquid* phase, we introduce the relative terminal rates defined, respectively, as $1 - V_s^\infty/V_{s,0}^\infty$ and $1 - V_l^\infty/V_{l,0}^\infty$, where the subscript 0 indicates the values when no magnetic field is applied ($B_0 = 0$). Figures 5(c) and 5(d) show a log-log representation of the relative terminal rates as a function of the magnetogravitational number Ψ. For both the *solid* and the *liquid* phase, the trends are reasonably fitted by a power law such that

$$1 - \frac{V_{s/l}^\infty}{V_{s/l,0}^\infty} = a_{s/l}\Psi^{b_{s/l}}, \tag{10}$$

with $a_s = 0.21 \pm 0.08$ and $b_s = 0.19 \pm 0.08$ for the *solid* phase and with $a_l = 0.12 \pm 0.01$ and $b_l = 8.1 \times 10^{-2} \pm 0.04$ for the *liquid* phase.

These trends reveal that the influence of the magnetic field is significantly stronger in hindering the liquefaction of the *solid* phase, than in hindering the growth rate of the *liquid* phase. This could be expected considering that in the more dilute *liquid* phase the interparticle distance is larger than in the compact *solid* phase where particles are in contact with each other. The induced magnetic particle-particle interactions are then reduced in the *liquid* phase which is indeed found to be marginally affected by the applied magnetic field. An interesting question then concerns the evolution of the particle concentration (and hence of the interparticle distance)

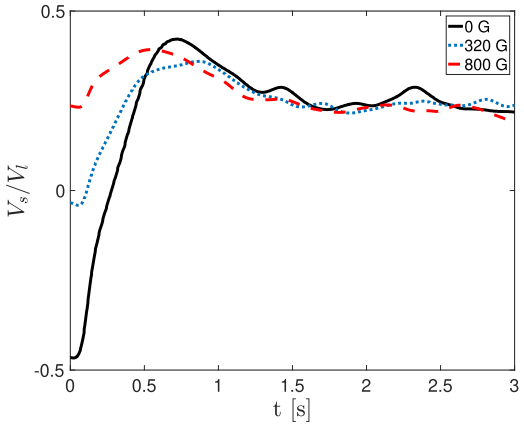

FIG. 6. Evolution with time of the *solid* to *liquid* rate ratio. In the terminal steady state, the *solid*-to-*liquid* rate ratio reaches an asymptotic value of the order of 0.25, independent of the magnetic field amplitude, indicating that the *liquid* phase is about four times more dilute than the *solid* phase.

in the *liquid* phase. This particle concentration results from the balance between the particles being supplied from the *liquefaction* of the *solid* phase and of the growth with time of the *liquid* area $A_l(t)$ as the *liquid* phase develops. We investigate this balance in the next subsection.

2. Particle concentrations in the solid and liquid phases

Let ρ_l and ρ_s be the particle concentration (number density) in the *liquid* and the *solid* phase, respectively. The particle concentration ρ_s is assumed to be constant and fixed by the compacity of the initial pack. Initially, the *liquid* phase is empty and emerges when the *solid* phase starts *liquefying*. The particle concentration in the *liquid* phase is therefore expected to have a nontrivial time evolution.

Keeping in mind that the cell is sealed, and hence the total number N_p of particles remains constant, the concentration in both phases can be directly related to the rates of *liquefaction* of the *solid* phase V_s and the rate V_l at which the *liquid* phase grows. Assuming that all particles remain either in the *liquid* or the *solid* phase (this approximation neglects the few particle blobs eventually detaching from the *liquid* phase) and that the concentration within each phase is relatively homogeneous, we can indeed write

$$N_p = \rho_l(t)A_l(t) + \rho_s(t)A_s(t). \tag{11}$$

The conservation of the total number of particles then imposes $dN_p/dt = 0$, which, considering Eq. (11) and assuming that ρ_s remains constant, leads to

$$\frac{V_s(t)}{V_l(t)} = \Gamma_{ls}(t) + \frac{d\Gamma_{ls}(t)}{dt}\frac{A_l(t)}{V_l(t)}, \quad \text{with} \quad \Gamma_{ls}(t) = \frac{\rho_l(t)}{\rho_s(t)}. \tag{12}$$

This relation directly links the *liquid* to *solid* concentration ratio Γ_{ls} to the corresponding areas and growth rates and in particular to the *solid* to *liquid* rate ratio $V_s(t)/V_l(t)$, which is represented in Fig. 6. In principle, Eq. (12) is a simple differential equation for Γ_{ls} with empirically known time dependent coefficients $(V_s(t)/V_l(t)$ and $A_l(t)/V_l(t)$, which are directly accessible from the measurements), from which we could derive the time evolution of Γ_{ls}. We focus here though on the long term asymptotic behavior, where the ratio $V_s(t)/V_l(t)$ is constant, and found to be of the order of $V_s^\infty/V_f^\infty \approx 0.25$ independently of the amplitude of the applied magnetic field (see Fig. 6). In this stationary regime, the solution of Eq. (12) is $\Gamma_{ls}^\infty = V_s^\infty/V_f^\infty$, hence $\Gamma_{ls}^\infty \approx 0.25$ independently of the amplitude of the applied magnetic field. This means that the *liquid* phase is about four times more dilute than the *solid* phase, and that the particle average concentration in the *liquid* phase is not affected by the presence of the magnetic field.

V. DISCUSSION AND CONCLUSION

Our experiments reveal that, even if the magnetogravitational numbers investigated in the present study remains relatively low ($\Psi < 0.6$), measurable effects are still observed regarding the impact of an applied magnetic field on the terminal decompaction rate under gravity of a pack of paramagnetic particles. Overall, the influence of an increasing magnetic field on the terminal dynamics of the decompaction of the *solid* pack exhibit several interesting features:

(1) The terminal *liquefaction* rate is reduced by the magnetic field and so is the growth rate of the *liquid* phase, although the impact of the magnetic field on the *liquid* phase remains marginal;

(2) The terminal concentration of the *liquid* phase is about a quarter that of the *solid* phase and does not depend on the applied magnetic field.

These trends can be qualitatively interpreted in terms of magnetic induced interactions between the particles in the *solid* phase. The reduction of the terminal *liquefaction* rate with magnetic field suggests a stabilizing effect of the magnetic field on the *solid* pack. A plausible origin could be the formation of chain-forces of particles sustained by attractive magnetic interactions reinforcing the global cohesion of the pack of particles. Finally, the independence of particles concentration in the *liquid* phase very likely reveals that when the particles are sufficiently dilute the typical interparticle distance is so that the magnetic interaction between induced dipoles becomes negligible compared to gravity and hydrodynamic interactions. In such situation, the magnetic field then is not expected to have any significant impact on the inner structure of the dilute *liquid* phase.

While the previous conclusions on the terminal dynamics of the decompaction of the *solid* pack are firmly established from our experimental results, an interesting point during the initial phase should deserve further investigation. Indeed, our analysis shows that, in the initial phase, the *liquefaction* is accelerated in presence of the magnetic field. The origin of the initial acceleration of the decompaction is still speculative but may result from the vertical repulsion between parallel induced dipoles from successive layers in the initially compact *solid* phase which could promote the initial destabilization of the *solid*-water interface. Thus loosened, particles in the interface could then self-organize to form the stabilizing chain-forces aforementioned.

The study of paramagnetic particles still deserves further developments. The proposed qualitative scenario for the decompaction process investigated in the present work

suggests indeed that most of the action of the magnetic field affects primarily the *solid* phase and the *solid-liquid* interface, while the *liquid* phase itself remains mostly insensitive to the applied field. One could then expect a clear signature of the magnetic field on the fingering (Rayleigh-Taylor like) instability occurring in the early stage of the decompaction at the interface between the *solid* phase and the water [20,21,24]. The scenario where the magnetic field would tend to increase the cohesion of the pack by magnetically induced chain-forces can be expected to act as an enhanced effective surface tension of the interface, with a possible stabilizing effect regarding the fingering instability. In the continuity of the present study, we would like to study the fingering instability, by a systematic investigation of the structure and the dynamics of the *solid-liquid* interface (to extract information on the wavelength and growth rate of the instability) as a function of the amplitude of the applied magnetic field. Finally a natural extension of this work would be to using ferromagnetic particles (rather than paramagnetic) to reach magnetogravitational numbers of the order of unity at reasonable seeding densities. Ferromagnetic particles would indeed allow to reach regimes with particle-particle interactions of similar amplitude to the one of the hydrodynamic forces, thus strongly affecting the dynamics of the *liquid* phase.

ACKNOWLEDGMENTS

This work benefited from the financial support of the Project IDEXLYON of the University of Lyon in the framework of the French program "Programme Investissements d'Avenir" (ANR-16-IDEX-0005). We thank Damien Leroy for helping us with the SQUID measurements to determine the magnetic susceptibility of our particles.

[1] M. R. Maxey and J. J. Riley, Equation of motion for a small rigid sphere in a nonuniform flow, Phys. Fluids **26**, 883 (1983).

[2] N. M. Qureshi, M. Bourgoin, C. Baudet, A. Cartellier, and Y. Gagne, Turbulent Transport of Material Particles: An Experimental Study of Finite Size Effects, Phys. Rev. Lett. **99**, 184502 (2007).

[3] N. M. Qureshi, U. Arrieta, C. Baudet, A. Cartellier, Y. Gagne, and M. Bourgoin, Acceleration statistics of inertial particles in turbulent flow, Eur. Phys. J. B **66**, 531 (2008).

[4] R. Volk, E. Calzavarini, G. Verhille, D. Lohse, N. Mordant, J.-F. Pinton, and F. Toschi, Acceleration of heavy and light particles in turbulence: Comparison between experiments and direct numerical simulations, Physica D **237**, 2084 (2008).

[5] E. Calzavarini, R. Volk, M. Bourgoin, E. Leveque, J. F. Pinton, and F. Toschi, Acceleration statistics of finite-sized particles in turbulent flow: The role of Faxen forces, J. Fluid Mech. **630**, 179 (2009).

[6] F. Toschi and E. Bodenschatz, Lagrangian properties of particles in turbulence, Annu. Rev. Fluid Mech. **41**, 375 (2009).

[7] M. Uhlmann, An immersed boundary method with direct forcing for the simulation of particulate flows, J. Comput. Phys. **209**, 448 (2005).

[8] M. Uhlmann and A. Chouippe, Clustering and preferential concentration of finite-size particles in forced homogeneous-isotropic turbulence, J. Fluid Mech. **812**, 991 (2017).

[9] C. E. Brennen, *Fundamentals of Multiphase Flow* (Cambridge University Press, Cambridge, UK, 2005).

[10] C. T. Crowe, T. R. Troutt, and J. N. Chung, Numerical models for two-phase turbulent flows, Ann. Rev. Fluid Mech. **28**, 11 (1996).

[11] D. A. Drew, Mathematical modeling of two-phase flow, Annu. Rev. Fluid Mech. **15**, 261 (1983).

[12] R. H. Davis and A. Acrivos, Sedimentation of noncolloidal particles at low Reynolds numbers, Annu. Rev. Fluid Mech. **17**, 91 (1985).

[13] H. M. Jaeger, S. R. Nagel, and R. P. Behringer, Granular solids, liquids, and gases, Rev. Mod. Phys. **68**, 1259 (1996).

[14] R. T. Bonnecaze, H. E. Huppert, and J. R. Lister, Particle-driven gravity currents, J. Fluid Mech. **250**, 339 (1993).

[15] E. Guazzelli and J. Hinch, Fluctuations and instability in sedimentation, Annu. Rev. Fluid Mech. **43**, 97 (2011).

[16] R. A. Bagnold, Experiments on a gravity-free dispersion of large solid spheres in a Newtonian fluid under shear, Proc. R. Soc. London Ser. A **225**, 49 (1954).

[17] G. K. Batchelor, Sedimentation in a dilute dispersion of spheres, J. Fluid Mech. **52**, 245 (1972).

[18] G. K. Batchelor and R. W. Janse Van Rensburg, Structure formation in bidisperse sedimentation, J. Fluid Mech. **166**, 379 (1986).

[19] A. Lange, M. Schröter, M. Scherer, A. Engel, and I. Rehberg, Fingering instability in a water-sand mixture, Eur. Phys. J. B **4**, 475 (1998).

[20] C. Völtz, W. Pesch, and I. Rehberg, Rayleigh-Taylor instability in a sedimenting suspension, Phys. Rev. E **65**, 011404 (2001).

[21] J. Vinningland, Ø. Johnsen, E. Flekkøy, R. Toussaint, and K. J. Måløy, Experiments and simulations of a gravitational granular flow instability, Phys. Rev. E **76**, 051306 (2007).

[22] J. W. S. Rayleigh, Investigation of the character of the equilibrium of an incompressible heavy fluid of variable density, Proc. London Math. Soc. **14**, 170 (1883).

[23] G. Taylor, The instability of liquid surfaces when accelerated in a direction perpendicular to their planes. I, Proc. R. Soc. London. ser. A **201**, 192 (1950).

[24] J. L. Vinningland, Ø. Johnsen, E. G. Flekkøy, R. Toussaint, and K. J. Måløy, Size invariance of the granular Rayleigh-Taylor instability, Phys. Rev. E **81**, 041308 (2010).

[25] The concentration of the liquid phase is four times lower than the closed packed concentration of the solid phase, as shown in Sec. IV B; the interparticles distance in the liquid phase is thus of the order of 1 particle diameter. This guides *a posteriori* the size of the Gaussian convolution kernel width of 1.5 particle diameter; and we checked that the robustness of our results when the convolution width was varied between 1 and 2 particle diameters.